remote sensing

IMPACT FACTOR 5.0

CITESCORE 7.9

Article

# The Extreme Rainfall Events of the 2020 Typhoon Season in Vietnam as Seen by Seven Different Precipitation Products

Giacomo Roversi, Marco Pancaldi, William Cossich, Daniele Corradini, Thanh Thi Nhat Nguyen, Thu Vinh Nguyen and Federico Porcu'

MDPI

https://doi.org/10.3390/rs16050805

*remote sensing*

MDPI

*Article*

# The Extreme Rainfall Events of the 2020 Typhoon Season in Vietnam as Seen by Seven Different Precipitation Products

**Giacomo Roversi [1,2], Marco Pancaldi [1], William Cossich [1], Daniele Corradini [1], Thanh Thi Nhat Nguyen [3], Thu Vinh Nguyen [4] and Federico Porcu' [1,*]**

[1] Department of Physics and Astronomy "Augusto Righi", University of Bologna (UNIBO), 40126 Bologna, Italy; giacomo.roversi3@unibo.it (G.R.); wcossich@gmail.com (W.C.)
[2] Institute of Atmospheric Sciences and Climate (ISAC), National Research Council (CNR), 00133 Rome, Italy
[3] University of Engineering and Technology, Vietnam National University (VNU), Hanoi 100000, Vietnam; thanhntn@vnu.edu.vn
[4] National Centre for Hydro-Meteorological Network (NCN), The Viet Nam Meteorological and Hydrological Administration (VNMHA), Hanoi 100000, Vietnam; nvthu@monre.gov.vn
* Correspondence: federico.porcu@unibo.it

**Abstract:** A series of typhoons and tropical storms have produced extreme precipitation events in Vietnam during the first part of the 2020 monsoon season: events of this magnitude pose significant challenges to remote sensing Quantitative Precipitation Estimation (QPE) techniques. The weather-monitoring needs of modern human activities require that these challenges be overcome. In order to address this issue, in this work, seven precipitation products were validated with high spatial and temporal detail against over 1200 rain gauges in Vietnam during six case studies tailored around the most intense events of 2020. The data sources included the Vietnamese weather radar network, IMERG Early run and Final run, the South Korean GEO-KOMPSAT-2A and Chinese FengYun-4A geostationary satellites, DPR on board the GPM-Core Observatory, and European ERA5-Land reanalysis. All products were resampled to a standardized 0.02° grid and compared at hourly scale with ground stations measurements. The results indicated that the radars product was the most capable of reproducing the information collected by the rain gauges during the selected extreme events, with a correlation coefficient of 0.70 and a coefficient of variation of 1.38. However, it exhibited some underestimation, approximately 30%, in both occurrence and intensity. Conversely, geostationary products tended to overestimate moderate rain rates (FY-4A) and areas with low precipitation (GK-2A). More complex products such as ERA5-Land and IMERG failed to capture the highest intensities typical of extreme events, while GPM-DPR showed promising results in detecting the highest rain rates, but its capability to observe isolated events was limited by its intermittent coverage.

**Keywords:** Vietnam; precipitation; satellite; rain gauge; AWS; weather radar; QPE validation; IMERG; GEO-KOMPSAT-2A; FengYun-4A



**Citation:** Roversi, G.; Pancaldi, M.; Cossich, W.; Corradini, D.; Nguyen, T.T.N.; Nguyen, T.V.; Porcu', F. The Extreme Rainfall Events of the 2020 Typhoon Season in Vietnam as Seen by Seven Different Precipitation Products. *Remote Sens.* **2024**, *16*, 805. https://doi.org/10.3390/rs16050805

Academic Editor: Yuriy Kuleshov

Received: 28 December 2023
Revised: 19 February 2024
Accepted: 20 February 2024
Published: 25 February 2024



## 1. Introduction

In the months between August and November 2020, Central Vietnam was inundated with many consecutive tropical depressions and typhoons, leading to extensive flooding and landslides. This catastrophic event claimed the lives of over 240 people, left more than 500 injured, and caused approximately USD 1.5 billion in direct damages, only for the month of October 2020 [1,2]. The region saw a combination of numerous weather systems: the Inter Tropical Convergence Zone combining with cold air produced in October the tropical storms Linfa, Nangka and Saudel and the typhoon Molave, which was one of the most devastating typhoons making landfall in Vietnam in decades. They were anticipated by tropical storms Sinlaku and Noul at the beginning of August 2020 and in the middle of September 2020, respectively, and were followed by the typhoon Goni and tropical storms Atsani and Vamco in the first half of November 2020. All weather systems originated in the

Pacific Ocean and reached Vietnam from the sea traveling west [2]. The effects of typhoon landfalls were compounded by the strong convection generated by the orographic lift of the eastern (windward) side of the Trungson mountain range in Central Vietnam [1].

Quantitative Precipitation Estimation (QPE) products with a high level of spatial and temporal detail (high resolution), the shortest lead time available (low latency), and wide coverage (regional to global) are relevant to a wide class of users, e.g., to modern agriculture or, looking at meteorological extremes, to early warning services. Nowadays, numerous QPE products are publicly available and accessible on a global scale, at different spatial and temporal resolutions. Most of them rely on remote sensing information from satellites in Low Earth Orbit (LEO) or Geostationary Orbit (GEO).

However, during extreme events like these ones, QPE through remote sensing techniques is a particularly hard task, due to known shortcomings [3]. It is therefore of great interest to see how different precipitation products differently describe rainfall during intense events. A comprehensive analysis of the detection and estimation capabilities of the products, which is commonly referred to as their error structure, is crucial knowledge to the end users in order to extract the most information from each of them or choose between them. Consequently, extensive ground validation programs are usually part of satellite mission activities [3,4], and they continue to be the primary focus of international working groups [5].

In recent years, numerous intercomparison and validation initiatives have been conducted in tropical regions [6,7] and in Southeast Asia [8–10] to evaluate the suitability of satellite precipitation products for various quantitative applications, particularly in agriculture and hydrology. These efforts have focused on the utilization of globally available satellite precipitation products in hydrological modeling for transboundary and inadequately monitored river catchments, such as the Mekong River Basin. The findings indicate satisfactory performance in describing river discharge at monthly scales when using these global satellite precipitation products. However, the evaluation revealed lower values of the Nash–Sutcliffe Efficiency (NSE) when assessing daily-scale river discharge [11,12]. Bias correction techniques can be employed to enhance the accuracy of global satellite precipitation products by incorporating local gauge-based data [13]. This approach proved to be beneficial in simulating streamflow in mountainous catchments [14,15], delivering promising results at both daily and monthly scales. In fact, it surpassed the conventional gauge-only approach [16,17]. Satellite products have also been utilized in crop simulation models, demonstrating favorable performance at monthly scales. However, their accuracy diminished considerably when applied to decadal and daily values [10]. Various validation studies conducted in Southeast Asia have examined the compatibility between daily satellite products and rain gauge data [18,19]. These studies highlight the potential benefits of implementing bias correction techniques to enhance the quantitative alignment of rain rate values.

Looking at Vietnam, multiple evaluations have been conducted in recent years to assess various precipitation products across different regions of the country. These studies utilized established reference datasets or the Vietnam Gridded Precipitation (VnGP) dataset, focusing on the performance of specific products, such as the IMERGv6 Final run [20], GSMaP [21] and TRMM3B42 [18]. These evaluations primarily concentrated on specific regions of Vietnam during the rainy season, including the northern region, Central Coast, and Central Highlands. They reported high correlations, ranging from 0.75 to 0.93, for daily and monthly average precipitation when compared to reference datasets or the VnGP. For instance, a study [22] evaluated the TRMM3B42 products (v7 and RT) over the Red-Thai Binh river basin, while another [23] compared multiple products (GPM TRMM, CHIRPS, GSMaP, and CMORPH) with ground station data in the Ca river basin for the period 2015–2017. Both studies found a high correlation in monthly average precipitation, with a correlation coefficient (CC) of 0.93, even at this larger scale. More recently, two studies [24,25] independently evaluated eight and six long-term satellite-based precipitation products over six and eleven river basins in Vietnam at both monthly and daily scales for

hydrological applications. Their findings indicate that the IMERG-Final run performed best among the examined candidates, particularly in representing the derived flood peaks. Overall, these evaluations provide valuable insights into the performance of precipitation products in different regions of Vietnam, demonstrating strong correlations, particularly for monthly average precipitation values.

It is worth noting that the existing literature focuses on validation and comparison exercises that are conducted at coarse resolution (product native or watersheds), and integrating over longer periods (day to month). Moreover, they are generally not focused solely on heavy rainfall events. In this work, we instead aim to specifically address extreme conditions, related to the 2020 typhoon season. At the same time, we want to assess precipitation products at a finer spatial and temporal resolution than the previous works in the literature, pushing the product design limits, trying to meet user demand.

The aim of this study is therefore to assess the accuracy of local and global precipitation products available over Vietnam during extreme weather periods at high resolution and analyze their error characteristics through mutual comparison and validation with ground reference data.

Specifically, we examined seven different data sources against a ground-based reference derived from rain gauges. We utilized products from the Dual Frequency Precipitation Radar on board the GPM-Core Observatory satellite [26], the estimates from infrared sensors on board the Chinese FengYun-4A and South Korean GEO-KOMPSAT-2A geostationary satellites [27], as well as the multi-satellite products from IMERG [28] and a ground-based product such as the weather radar QPE. Moreover, we considered the ERA5-Land reanalysis [29,30], which is the "Land" version of the fifth generation of the ECMWF Reanalysis, as an additional product based on a different approach.

The data sources utilized in this study are detailed in Section 2, while the comparison methods are explained in Section 3, including the description of the precautions taken to ensure a consistent intercomparison. Subsequently, the actual results of the intercomparison are presented in Section 4, followed by a comprehensive discussion in Section 5. Finally, Section 6 concludes the study by summarizing the key findings.

## 2. Data

This study incorporates seven precipitation products and a quantitative precipitation reference over Vietnam (see Table 1), which can be categorized into five different types of data sources:

- Ground-based instruments: this includes rain gauges obtained from automatic weather stations and weather radars.
- Precipitation estimations from geostationary satellites (GEO): the study utilizes data from the Advanced Geo-synchronous Radiation Imager (AGRI) on board the Chinese FengYun-4A satellite and the Advanced Meteorological Imager (AMI) on board the South Korean GEO-KOMPSAT-2A satellite.
- Precipitation estimation from a space-borne radar on a low Earth orbit (LEO) platform: the Dual-frequency Precipitation Radar on board the NASA-JAXA GPM-CO satellite.
- Multi-satellite products with different levels of calibration and latency: specifically, the Integrated Multi-satellitE Retrievals for GPM (IMERG) Early and Final runs.
- Model reanalysis: the "Total precipitation" variable of the ERA5-Land product by ECMWF (European Centre for Medium-Range Weather Forecasts).

These diverse data sources enable a comprehensive analysis of precipitation patterns and their estimation accuracy in Vietnam.

**Table 1.** Summary of the main characteristics of the precipitation products. In the last row are also presented the characteristics of the common interpolation grid over which the comparisons are carried out in this work.

| Dataset | Period | Grid Resolution | Temporal Sampling | Coverage | Data Source | Latency |
|---|---|---|---|---|---|---|
| AWS (rain gauges) | 2008–present | point (avg. dist.: 8.6 km) | 10 min/1 h | country-wide | tipping bucket | ∼10 min/ 30 min–1 h |
| Radars | 2019–present | 1 km | 1 h | country-wide | C- and S-band | 15–30 min |
| GPM-DPR | 2014–present | 5 km | ∼1 overp./day | 245 km swath (global) | DPR (Ku + Ka) | 1 day |
| FY-4A | 2017–present | 4 km (nadir) | 1 h/3 h/6 h | full disk | VIS-IR | NRT |
| GK-2A | 2018–present | 2 km (nadir) | 10 min | full disk | IR + DPR | NRT |
| IMERG Early run | 2000–present | 0.1° × 0.1° | 30 min | global | MW + DPR + IR | 4 hours |
| IMERG Final run | 2000–present | 0.1° × 0.1° | 30 min | global | MW + DPR + IR + rain gauges | 3.5 months |
| ERA5-Land | 1950–present | ∼9 km | 1 h | global | ECMWF model | 2 to 3 months |
| This work | August 2020–November 2020 | 0.02° × 0.02° | 1 h | from 7°N–101°E to 24°N–111°E | 8 different sources | - |

### *2.1. Ground Reference Data: Automatic Rain Gauge Stations*

The rain gauge network in Vietnam is operated and managed by multiple stakeholders, including the Vietnam Meteorological and Hydrological Administration (VNMHA). This extensive network comprises approximately 1300 automatic weather stations (AWS) spread across the country (see Figure 1). However, there are some density fluctuations and occasional interruptions in the network, resulting in around 800–900 active and quality controlled rain gauges at any given time. These rain gauges collect readings every 10 min. For the purpose of this study, the recorded rain rates were accumulated to compute hourly averages in millimeters per hour (mm/h), representing the total accumulated rainfall for each hour. On average, the minimum distance to the nearest rain gauge station is approximately 8.6 km.

### *2.2. Ground Weather Radar Precipitation Product*

In 2020, Vietnam's ground weather radar network consisted of five dual-polarization radars located in cities including Viet Tri, Nha Trang, Quy Nhon, Pleiku, and Pha Din Pass. Additionally, there were three single-polarization C-band radars in Dong Ha, Tam Ky, and Nha Be, as well as two single-polarization S-band radars in Phu Lien and Vinh. The data used in this study were collected from these 10 radar sites, which was partially inherited from the results of the Vietnam National Research Project with the code ĐTĐL.CN-58/21. Before incorporating the radar data into the Quantitative Precipitation Estimation (QPE) calculation, a quality control process was conducted to filter out basic errors. The radar precipitation product was derived from one-hour accumulated radar intensity, using the original method developed by the Japan Meteorological Agency (JMA) [31], with adaptations for the Vietnamese region by the Japan Weather Association (JWA) [32] and the National Centre for Hydro-Meteorological Network (NCN). These adaptations involved decoding the input raw radar data and making parameter corrections. The radar product provides hourly coverage for nearly all of mainland Vietnam, with a resolution of 1 km.

The areas with the best overlap between instruments are in the north, while the density of instruments is lower in the middle and southern parts of the country (Figure 1).

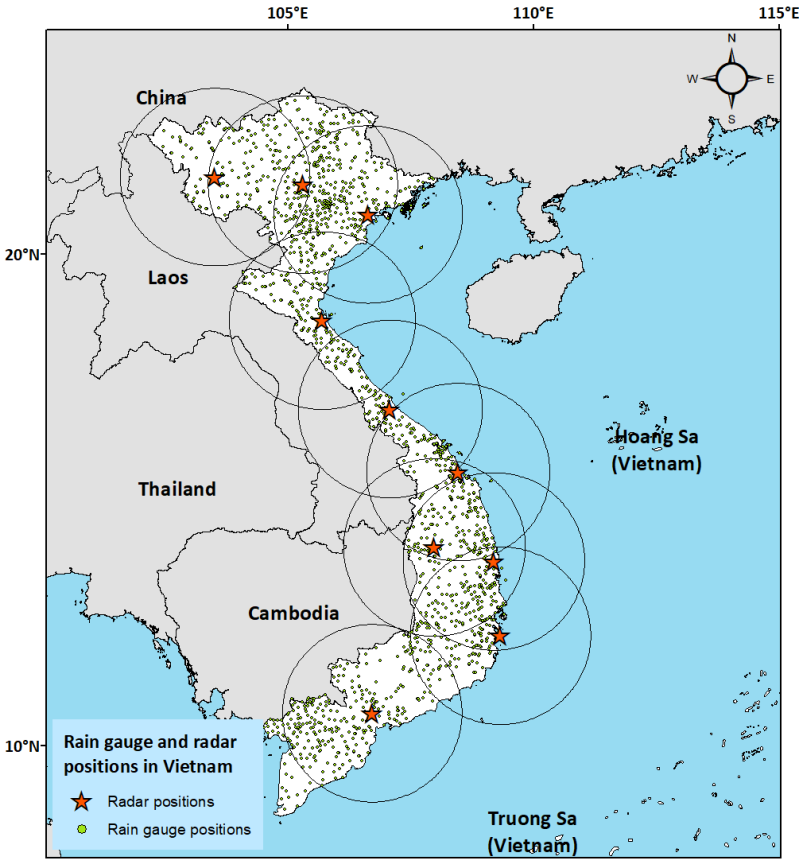


**Figure 1.** Map of Vietnam with AWS and radar locations.

### *2.3. Space-Borne Radar Product: GPM-DPR*

The Dual-frequency Precipitation Radar (DPR) is an active sensor on board the GPM Core Observatory satellite, operating in the Ku (13.6 GHz) and Ka (35.5 GHz) frequency bands. The 2ADPR Level-2 product (version V07A) utilizes the reflectivity measurements from both frequency bands to estimate the precipitation rate at the surface. The "precipRateESurface" variable (5 km resolution at nadir) of the 2ADPR product is utilized in this work since it is considered valuable for comparison with ground-based data [26,33].

### *2.4. Geostationary Satellite-Based Products: GEO-KOMPSAT-2A and FengYun-4A*

Currently, three geostationary weather satellites observe Vietnam: the Chinese Fengyun-4A located at longitude 104.7°E, the South Korean GEO-KOMPSAT-2A positioned at longitude 128.2°E, and the Japanese Himawari-8 situated at longitude 140°E.

The geostationary satellites mentioned in this study host similar sensors, with comparable channels and ground resolutions. However, it is important to note that the Chinese and South Korean agencies employ different algorithms for precipitation retrieval. As for Himawari-8, no official precipitation product has been released yet, and as a result, it is not included in this study. However, it is worth mentioning that there is promising ongoing research using random forests [34] that has shown good results in Japan and is currently being replicated in the context of Vietnam.

#### 2.4.1. GEO-KOMPSAT-2A

The GEO-KOMPSAT-2A (Geostationary Korea Multi-Purpose Satellite 2A, or GK-2A) is a geostationary satellite operated by the Korea Meteorological Administration (KMA),

National Meteorological Satellite Center (NMSC). It has been in operation at a longitude of 128.2°E since December 2018. On board the GK-2A, the Advanced Meteorological Imager (AMI) consists of 16 spectral channels, covering a range from visible to thermal infrared (with wavelengths between 0.47 and 13.3 μm). The spatial resolution of the infrared channels is 2 km at nadir, and the temporal resolution for the full disk area is 10 min. The rain rate estimation algorithm used by GK-2A utilizes brightness temperatures from five different bands (6.24 μm, 7.34 μm, 8.59 μm, 11.21 μm, 12.36 μm). It discriminates cloud types by applying predefined thresholds to cloud top height and thickness, then estimates precipitation intensity by a statistical matching of the probability density functions derived from recent GPM-DPR data. This approach thus leverages the information from the GPM-DPR to improve the accuracy of precipitation estimation from the GK-2A satellite [27]. The data utilized here come from the AMI Level-2 rainfall rate product ("AMI L2 RR"), obtained with the "GK2A_RR" algorithm, version 1.6.0.4. Technical documentation is available only in Korean [35].

#### 2.4.2. FengYun-4A

Fengyun-4A (FY-4A) is the first satellite of China's second-generation geostationary meteorological satellites [36]. It is operated by the National Satellite Meteorological Center (NSMC) under China Meteorological Administration (CMA). It is positioned at a longitude of 104.7°E. The precipitation estimate is derived from the Advanced Geosynchronous Radiation Imager (AGRI), which measures upward atmospheric radiance from 14 channels, covering a spectral range of 0.55 μm to 13.8 μm with 4 km nadir resolution [37]. The specific algorithms and procedures used by FY-4A are not publicly available, but the literature suggests that the current version lacks a calibration step, and future versions may incorporate radar measurements [27]. The precipitation product is called "FY4A AGRI L2 QPE", or "Quantitative Rainfall Rate Estimation of AGRI", and is generated by version 1.0 of the software.

### *2.5. Multi-Satellite Products and Model Reanalysis: IMERG and ERA5-Land*

#### 2.5.1. IMERG

The IMERG algorithm (version 3IMERGH_6.3) of the GPM Mission provides precipitation estimations at the Earth's surface by merging data from multiple satellites in both low and geostationary orbits, using the infrared (IR) and microwave (MW) parts of the spectrum. The available IMERG products (version V06B) include the Early run, Late run, and Final run. A comprehensive description of the IMERG algorithm can be found in [28]; the respective technical document is [38]. As we move from the Early run to the Final run, the calibration steps and quality controls become more structured, along with an increase in latency. The Early run, released after 4 h, relies solely on satellite data. The Late run, published 10 h after the Early run (with a latency of approximately 14 h), incorporates data from the satellite overpasses that were not available in the initial 4 h. The Final run, released after 3.5 months, includes calibration using the gauges of the Global Precipitation Climatology Centre (GPCC) monthly Monitoring Analysis. For this study, only the Early and Final runs were considered. The Early run represents an almost near real-time (NRT) merged product, while the Final run provides the most reliable satellite-based global precipitation estimate available in the area. The rainfall field used in this study is extracted from the "precipitationCal" variable, on a $0.1^\circ \times 0.1^\circ$ grid every hour.

#### 2.5.2. ERA5-Land

ERA5 is the state-of-the-art reanalysis product developed by the European Centre for Medium Range Weather Forecasts (ECMWFs) [39]. ERA5-Land, a component of ERA5, focuses specifically on land-related variables and provides a finer spatial resolution, with a grid spacing of approximately 9 km [30]. In this study, we consider the "Total Precipitation" variable from ERA5-Land, which has a temporal resolution of 1 h and a spatial resolution of 0.1°. The Total Precipitation product in ERA5-Land is derived from the sum of two

sources: the large-scale precipitation term, computed by the model at scales greater than the grid box, and the convective precipitation term, computed by the convective scheme within the ECMWF Integrated Forecasting System at spatial scales smaller than the grid box. To match the finer resolution of ERA5-Land, the precipitation field is interpolated from the original ERA5 resolution (approximately 31 km) to the ERA5-Land resolution using a linear interpolation method based on a triangular mesh [29].

### *2.6. Study Period: Heavy Rainfall Events between August and November 2020*

The analysis focused on specific periods when the tropical storms and typhoons made landfall over mainland Vietnam, to capture the occurrence of heavy precipitation, spanning a cumulative total of 29 days. The case studies were distributed across the months from August to November 2020, as shown in Table 2. A preliminary selection was based on official government data for yearly typhoons provided by the Disaster Management Policy and Technology Center (DMPTC), then the selection was refined using rain gauge data.

**Table 2.** Summary table of the six case studies considered for this work, selected around the main precipitation events of the 2020 typhoon season over Vietnam, with summary statistics of the reference precipitation seen by the rain gauge stations.

| Case ID | Start (Date) | End (Date) | Duration (Hours [Days]) | Wet Ratio (%) | Average Rain Rate (mm/h) | Std. Deviation (mm/h) | Maximum Rain Rate (mm/h) |
|---|---|---|---|---|---|---|---|
| 1 | 31 July | 3 August | 73 [3] | 36.2 | 3.27 | 4.95 | 61.6 |
| 2 | 16 September | 20 September | 97 [4] | 29.9 | 2.89 | 5.86 | 106.6 |
| 3 | 5 October | 11 October | 145 [6] | 26.2 | 5.10 | 8.31 | 209.4 |
| 4 | 14 October | 21 October | 169 [7] | 31.2 | 3.83 | 6.83 | 96.8 |
| 5 | 27 October | 1 November | 121 [5] | 26.6 | 2.70 | 5.93 | 111.8 |
| 6 | 13 November | 17 November | 97 [4] | 23.6 | 1.48 | 3.63 | 289.7 |
| Whole dataset | August 2020 | November 2020 | 702 [29] | 28.8 | 3.49 | 6.57 | 289.7 |

Using a threshold of 0.2 mm/h (see Section 4.2 and Section S1 of the Supplementary Material for more insight about the threshold selection) to differentiate between wet and dry samples, the AWS recorded a total of 174,675 wet samples of the total reference data points, which are 610,120, counting both the temporal and spatial dimensions (see Section 3.2), for a wet ratio of 28.8% (Table 2).

The average rainfall value measured was 3.49 mm/h, with a standard deviation of 6.57 mm/h. The maximum recorded value reached 289.7 mm/h. Case-specific values are shown in Table 2. Hourly average rainfall rates surpassed 200 mm/h only during case study numbers 3 and 6. The majority of the rainfall values remained below 100 mm/h. The average values across the country never exceeded 6 mm/h. Notably, case number 6 shows the highest maximum but the lowest average rain rate.

Figure 2 displays the spatial distribution of the AWS data during the selected 29 days, time-aggregated with four statistics and utilizing a linear, Euclidean-distance based nearest neighbor algorithm to create space-continuous maps for qualitative display purposes. The precipitation exhibits a distinct regional pattern, mainly governed by the spatial distribution of the 2020 typhoon trajectories (see Sections S2 and S3 of the Supplementary Material). The central part of Vietnam experienced the highest number of wet hours (Figure 2a), while the northeastern and northwestern mountains were comparatively drier regions, consistent with the local climatology [40]. In the narrow strip between 16°N and 18°N are concentrated the highest mean, maximum and standard deviation values (Figure 2b–d).

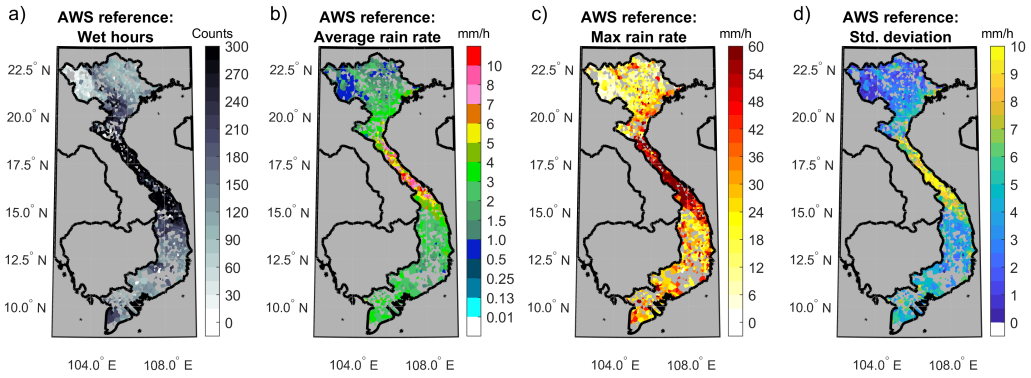


**Figure 2.** Map of various statistics for the AWS reference dataset. (**a**) Number of wet hours for each grid box. (**b**) Average rain rate (mm/h) among wet hours. (**c**) Maximum rain rate (mm/h) among wet hours. (**d**) Standard deviation of the rain rate (mm/h) among wet hours.

### *2.7. Data Availability and Coverage*

All the precipitation products utilized in this study have different spatial and temporal resolutions. Spatially, the resolutions range from 1 km for the radar data to 10 km for the IMERG and ERA5-Land products. Temporally, they range from 10 min to 1 h. Each product then also had its own temporary issues and outage periods. Table 3 provides aggregated information on the temporal coverage of each product with respect to the total hours considered (702). All products except GPM-DPR have levels of coverage always equal or higher than 90%. GPM-DPR coverage is so much lower (12%, corresponding to 84 h) and nonhomogeneous because the GPM Core satellite passes over the region only about once per day (see Table 1 and Section 2.3 for further details). All products show great stability except AWS, which present some fluctuations across the case studies.

**Table 3.** Summary table of the temporal coverage of all the considered products, in percentage with respect to the number of total time intervals, evaluated at the rain gauge locations.

| Case ID | Product Coverage (% of Time) | | | | | | | |
|---|---|---|---|---|---|---|---|---|
| | AWS | Radars | GK-2A | FY-4A | GPM-DPR | IMERG-Early | IMERG-Final | ERA5-Land |
| 1 | 90 | 100 | 100 | 100 | 4 | 100 | 100 | 99 |
| 2 | 97 | 100 | 100 | 98 | 8 | 100 | 100 | 99 |
| 3 | 95 | 100 | 100 | 100 | 9 | 100 | 100 | 98 |
| 4 | 98 | 100 | 100 | 100 | 15 | 100 | 100 | 99 |
| 5 | 94 | 100 | 100 | 100 | 25 | 100 | 100 | 99 |
| 6 | 97 | 100 | 100 | 100 | 9 | 100 | 100 | 99 |
| Whole dataset | 95 | 100 | 100 | 100 | 12 | 100 | 100 | 99 |

## 3. Methods

### *3.1. A Shared Spatial Grid for a Multi-Platform Analysis*

In order to perform the comparison between the various precipitation products sourced from different providers, it was necessary to homogenize the spatial and temporal resolutions. Temporally, the comparison was conducted at the minimum common time step of 1 h, in order to limit temporal interpolations. To perform the spatial matching, we converted all products to a grid finer than most of the analyzed products, in order to meet user requirements for high resolution and to check the sensitivity to extreme precipitation.

All data sources were re-projected onto a homogeneous spatial grid (see Figure 3), knowing that possible errors intrinsic to this process will contribute to the overall error. The grid had a 0.02° step in both latitude and longitude, which corresponds to approximately 2 km at the latitude of Vietnam, and a geographical extent from 7°N to 24°N and 101°E to 111°E.

Rain gauge measurements of the AWS reference were assigned to the grid boxes that corresponded to their actual locations. In cases where a grid box contained more than one station (45 occurrences), the measurements were averaged. Grid boxes without any station measurement were excluded from the quantitative analysis.

Eventually, a nearest neighbor algorithm was employed to fill the ungauged regions, only to create space-continuous rainfall maps for visualization purposes and qualitative analyses (Figures 2, 4 and 5), with no impact on the quantitative validation.

Figure 3 presents a sample snapshot of the hourly precipitation as seen by the rain gauge reference and the seven products, remapped on the common grid. In the graphical representation, the white color indicates zero rainfall intensity, while gray areas denote no data.

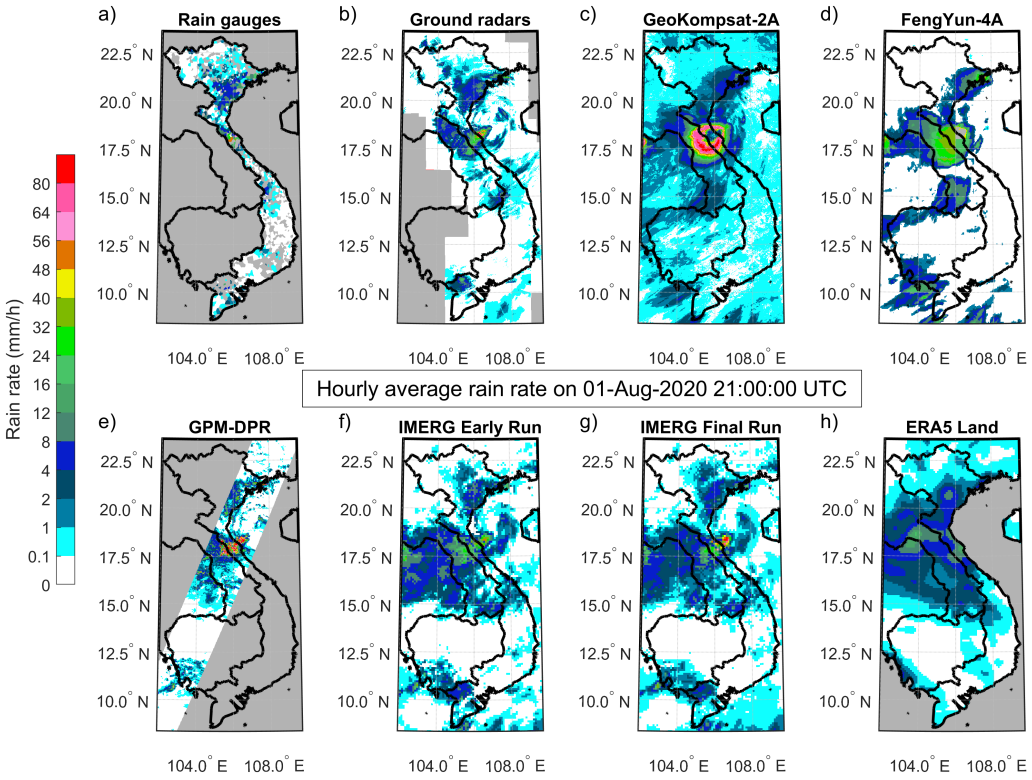


**Figure 3.** Products remapping output: intercomparison map of the 8 precipitation products for the same time interval (namely, 21.00 UTC of 1 August 2020). Grey grid boxes are the areas without any data. (**a**) AWS; (**b**) radars composite; (**c**) GEO-KOMPSAT-2A; (**d**) Fengyun-4A; (**e**) GPM-DPR; (**f**) IMERG-Early run; (**g**) IMERG-Final run; (**h**) ERA5-Land total precipitation.

### *3.2. Towards a Uniform Dataset: Products Intersection*

The main dataset for the analysis was created by considering the intersection of the availability of all products but GPM-DPR. This obviously produced a 27% smaller sample than the union of all available data but ensured the simultaneous presence of all sources at all times. This intersection was applied at the hourly scale, separately for each time interval. Thus, the spatial extent of the resulting dataset slightly varied over time, reflecting the fluctuations in the least populated product of each hour. The process was repeated including the GPM-DPR product, resulting in a second separate dataset of approximately 1% of the size of the main one. However, when looking at the characteristics of the precipitation measured by the AWS reference, the GPM-DPR subset is very similar to the overall dataset, with a wet fraction of 28.4% and an average rain rate of 3.89 mm/h.

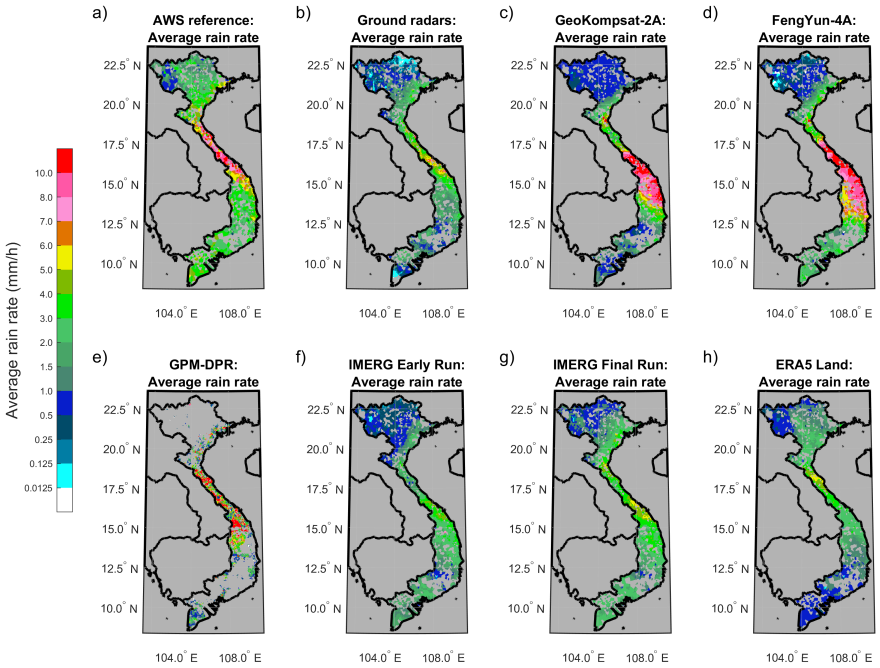


**Figure 4.** Maps of the average rain rates of all products over the common grid: (**a**) AWS; (**b**) radars; (**c**) GK-2A; (**d**) FY-4A; (**e**) GPM-DPR; (**f**) IMERG-Early run; (**g**) IMERG-Final run; (**h**) ERA5-Land.

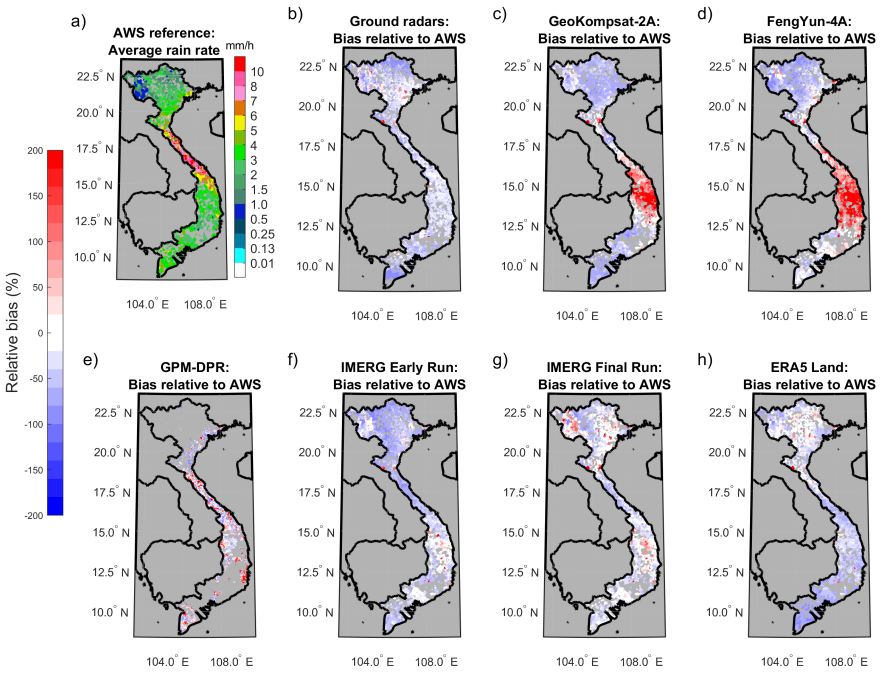


**Figure 5.** Maps of the bias of all products relative to the AWS reference product: (**a**) AWS (reference data); (**b**) radars; (**c**) GK-2A; (**d**) FY-4A; (**e**) GPM-DPR; (**f**) IMERG-Early run; (**g**) IMERG-Final run; (**h**) ERA5-Land.

The AWS dataset populated a maximum of 1394 grid boxes when projected onto the common grid (see Section 3.1). Their number was not constant due to fluctuations in the number of working stations, but most of the grid boxes contained valid measurements for more than 80% of the time. Only a small subset of stations (contained in 148 grid cells, around 10% of the total) provided valid readings for less than 50% of the time. With the aim of improving the quality of the dataset, these scarcely populated cells were removed from the AWS dataset. A general intersection of all grid boxes and time intervals ensured that the comparison between the products happened only over the grid boxes which contained

all spatial products and at least one rain gauge. A maximum of 1229 grid boxes per time interval were considered.

The resulting main dataset accounts for 610,120 data points (counting both temporal and spatial dimensions), while 4710 points make up the subset which includes GPM-DPR.

### *3.3. Error Metrics*

Several statistical indicators were used to perform comprehensive analysis. A set of five categorical indices was used to evaluate the detection capabilities of the products. In addition, six continuous scores were employed to assess the quality of the reconstructed rain fields at the rain gauge locations.

#### 3.3.1. Categorical Indices

Categorical indices are commonly utilized to assess the ability of a model or method to detect precipitation events. The classification of rain/no-rain was conducted by applying a threshold to the measured and estimated rainfall data. A $2 \times 2$ contingency matrix was then populated by comparing the occurrence of threshold-exceeding events between the reference (truth) and the products (estimates). Hits (H) and correct rejections (C) are located on the main diagonal, while misses (M) and false alarms (F) are positioned outside of it.

This study utilized several indices to evaluate the performance of the products. These indices include the probability of detection (POD), false alarm ratio (FAR), multiplicative BIAS (mBIAS), critical success index (CSI), and equitable threat score (ETS). Each index is derived from different elements of the contingency matrix. Table 4 provides a reference of these indices, including their definitions, ranges, and optimal values [41].

**Table 4.** Indices for the categorical metric [41]. They are expressed by combinations of the four elements of the contingency matrix: hits ($H$), misses ($M$), false alarms ($F$) and correct rejections ($C$). The expected random hits ($H_R$) are defined as $H_R = [(H + M) \times (H + F)]/[H + M + F + C]$.

| Name | Equation | Range of Values | Optimal |
|---|---|---|---|
| Probability of detection | $POD = H/(H + M)$ | [0 , 1] | (1) |
| False alarm ratio | $FAR = F/(H + F)$ | [0 , 1] | (0) |
| Multiplicative bias | $mBIAS = (H + F)/(H + M)$ | [0–∞] | (1) |
| Critical Success Index | $CSI = H/(H + M + F)$ | [0 , 1] | (1) |
| Equitable threat score | $ETS = (H - H_R)/(H + M + F - H_R)$ | $[-\frac{1}{3}$ , 1] | (1) |

#### 3.3.2. Continuous Indices

Continuous indices assess the quantitative accuracy of rainfall products by comparing each point estimate with its corresponding reference measurement. In this study, we employed well-established indices (defined in Table 5) to evaluate the performance of the products: the Pearson's correlation coefficient (CC), the normalized root mean square error or coefficient of variation (CV), the normalized mean error or bias (ME), and the normalized mean absolute error (MAE). In addition to these common metrics, we also calculated two more indices: the modified Kling–Gupta efficiency (mKGE) and $P_{50}$. These metrics provide further insights into the performance of the rainfall products.

The Kling–Gupta Efficiency [42], in its modified version by [43], is derived in a 3D space where the orthogonal dimensions represent the correlation coefficient (CC), the ratio between the global mean values of the product and reference fields ($\mu_e/\mu_o$, which is equivalent to $1 + ME$), and the ratio between the normalized standard deviations of each field ($\frac{\sigma_e/\mu_e}{\sigma_o/\mu_o}$). The mKGE is calculated as one minus the Euclidean distance from the obtained coordinates to the ideal point $(1, 1, 1)$. The mKGE score not only measures the goodness-of-fit between estimates and observations but also provides a deeper understanding of the Nash–Sutcliffe Efficiency (NSE) by examining its components [42].

The $P_{50}$ indicator represents the probability that an estimate will fall within plus or minus 50% of the actual measurement. It provides a practical evaluation of the overall

accuracy of a product by allowing for a reasonable level of deviation (50% in this case). This indicator acknowledges that high-resolution precipitation products may exhibit some variability, and conventional metrics may be less forgiving in assessing their performance. By considering a broader range of acceptable values, the $P_{50}$ indicator offers a more realistic assessment of the fitness of a product.

**Table 5.** Indices for the continuous metric. The letters $e$ and $o$ refer to the estimate and to the observed reference, respectively, $\sigma_{o,e}$ is the covariance of observation and estimate, $\sigma_o$ is a standard deviation, $\mu_o$ is an average, $\beta = \mu_e/\mu_o$ is the ratio of the averages, $\gamma = \frac{\sigma_e/\mu_e}{\sigma_o/\mu_o}$ is the ratio of the normalized standard deviations, and $n(x)$ is the number of occurrences of $x$.

| Name | Equation | Range of Values | Optimal |
|---|---|---|---|
| Correlation coefficient | $CC = \sigma_{o,e}/\sigma_o\sigma_e$ | $[-1\,,\,1]$ | (1) |
| Coefficient of variation | $CV = \sqrt{\frac{\Sigma(e_i-o_i)^2}{N}}/\mu_o$ | $[0\,,\,\infty]$ | (0) |
| Normalized mean error, or bias | $ME = \sum_i(e_i - o_i)/N\mu_o$ | $[-\infty\,,\,\infty]$ | (0) |
| Normalized mean absolute error | $MAE = \sum_i \lVert e_i - o_i \rVert/N\mu_o$ | $[0\,,\,\infty]$ | (0) |
| Modified Kling–Gupta efficiency | $mKGE = 1 - \sqrt{(CC-1)^2 + (\beta-1)^2 + (\gamma-1)^2}$ | $[-\infty\,,\,1]$ | (1) |
| Probability to have $e_i$ inside ±50% of $o_i$ | $P_{50} = n\left[e_i \mid (0.5 \times o_i) \le e_i \le (1.5 \times o_i)\right]/N$ | $[0\,,\,1]$ | (1) |

## 4. Results

The analysis begins by examining how the precipitation products are able to reproduce the average rainfall spatial pattern measured by the AWS reference and depicted in Figure 2b. This will appear in Section 4.1. The first quantitative analysis, presented in Section 4.2, involved the detection skills at hourly resolution across a fixed rain rate threshold of 0.2 mm/h. Then, the quantitative representativeness of the precipitation estimates was studied. A general outlook was provided in terms of probability density functions of the rainfall intensity (Section 4.3). The samples indicated as rain by the AWS reference were then compared against each corresponding one from the various products to evaluate the estimation accuracy (Section 4.4). Finally, the sensitivity to rainfall intensity was evaluated, varying the rain/no-rain threshold (Section 4.5).

### *4.1. Spatial Distribution of Average Values*

Figure 4 displays the maps where all hourly measurements are averaged (702 h total) for each grid box, after removing dry occurrences, while Figure 5 shows the respective biases to the AWS reference. The AWS reference is first presented in Figure 2b and is reiterated in Figures 4a and 5a for ease of comparison and interpretation with the other panels. The color gradient ranging from lighter to darker shades of red indicates increasing levels of overestimation, while the blue gradient indicates underestimation.

A key to interpret these results is to keep in mind that the northwestern part of Vietnam is mainly mountainous, while in the south, lowlands are prevalent (see Section S2 of the Supplementary Material). The central part of the country was the preferred landing zone for typhoons in 2020 (see Section S3 of the Supplementary Material).

All the products correctly identified the highest rainfall intensities in the central region of Vietnam, but there are notable variations among them. For instance, ERA5-Land indicates its maximum rainfall values located further north compared to the other six products. The geostationary products instead display maximum values that extend more towards the southern part of Vietnam, reaching as far south as 13°N; whereas other products such as radars show maximum values at a slightly higher latitude, around 15°N. The discrepancies in the numerical values of the geostationary estimates are particularly pronounced and concentrated in the central region of Vietnam. However, in the northern and southern parts of the country, the geostationary estimates align more closely with the other products. It is worth noting that the calibration process of IMERG, from the Early run

to the Final run, appears to have a greater impact on the northern region of the country (above 18°N) compared to other areas.

### *4.2. Rainfall Area Detection*

The rain/no-rain threshold was set at 0.2 mm/h based on a detailed analysis of the PDF of the rainfall products for low rain rates (shown in Section S1 of the Supplementary Material). This threshold of 0.2 mm/h is also the lowest common denominator of the instrumental resolution of the rain gauges.

Categorical scores are computed using a contingency matrix that tabulates the number of hits, misses, correct rejections, and false alarms (refer to Table 4) in relation to the occurrence of rain in the AWS data. An overview of the detection capabilities of the different products during the studied period is provided in Table 6.

**Table 6.** Statistical indicators for the categorical analysis. Products with the best and worst performance results for each score are indicated with bold and italic fonts, respectively (except for GPM-DPR, which does not share the same sample size). The ideal target scores are indicated in Table 4.

| Product | CSI | ETS | POD | FAR | mBIAS |
|---|---|---|---|---|---|
| Radars | **0.53** | **0.41** | 0.61 | **0.21** | 0.77 |
| GK-2A | 0.38 | *0.18* | 0.69 | *0.55* | 1.53 |
| FY-4A | *0.34* | 0.21 | *0.43* | 0.39 | 0.71 |
| IMERG-Early run | 0.40 | 0.25 | 0.55 | 0.41 | 0.92 |
| IMERG-Final run | 0.43 | 0.28 | 0.62 | 0.42 | **1.07** |
| ERA5-Land | 0.44 | 0.24 | **0.83** | 0.52 | *1.71* |
| GPM-DPR * | 0.55 | 0.45 | 0.61 | 0.15 | 0.72 |

* Sample size of GPM-DPR is ∼99% smaller than the other products', which instead all share the same one.

The GPM-DPR showed the highest performance in terms of Critical Success Index (0.55) and Equitable Threat Score (0.45), although it should be stressed that its sample size is only approximately 1% of the others. The radar products closely followed with a CSI of 0.53 and ETS of 0.41, demonstrating the strongest overall detection capabilities across the main dataset (i.e., not considering GPM-DPR). The remaining products lagged behind, particularly in terms of ETS. Both the ground-based radar and GPM-DPR products exhibited the same Probability of Detection (POD) at 0.61, similar mBIAS values (0.77 and 0.72, respectively), and low False Alarm Rates (FARs) at 0.21 and 0.15, respectively. The geostationary products, GK-2A and FY-4A, exhibit similar overall detection performance with CSI values below 0.4 and ETS values around or below 0.2. However, they differ in terms of mBIAS. GK-2A demonstrates a good Probability of Detection (POD) at 0.69 but overestimates rainfall occurrence by 53%. Conversely, FY-4A exhibits a lower False Alarm Rate (FAR) but only captures 43% of the measured precipitation occurrence. The IMERG products demonstrate modest detection performance, with CSI values slightly above 0.4 and ETS values below 0.3. The effects of calibration in the Final run are most noticeable in the POD and mBIAS, which nonetheless were good already. The FAR instead, which was above 0.4, did not show improvement through the calibration process, and was even slightly worse than the Early run. ERA5-Land exhibits the highest POD (0.83), at the expense of a high FAR at 0.52, which results in the worst mBIAS among all the products. This indicates an overestimation of precipitation occurrence by ERA5-Land.

### *4.3. Overall Distribution of the Estimated Rain Rates*

To evaluate the representativeness of the quantitative estimates of the products during the study period, only the subset with "wet" reference samples was considered. Firstly, it was verified whether the seven products were able to reproduce the distribution of the intensity of the reference rainfall. The probability density functions (PDFs) at the AWS

positions were calculated for all 702 h and 1229 grid points using a 2 mm/h binning, ranging from 1 to 200 mm/h (Figure 6).

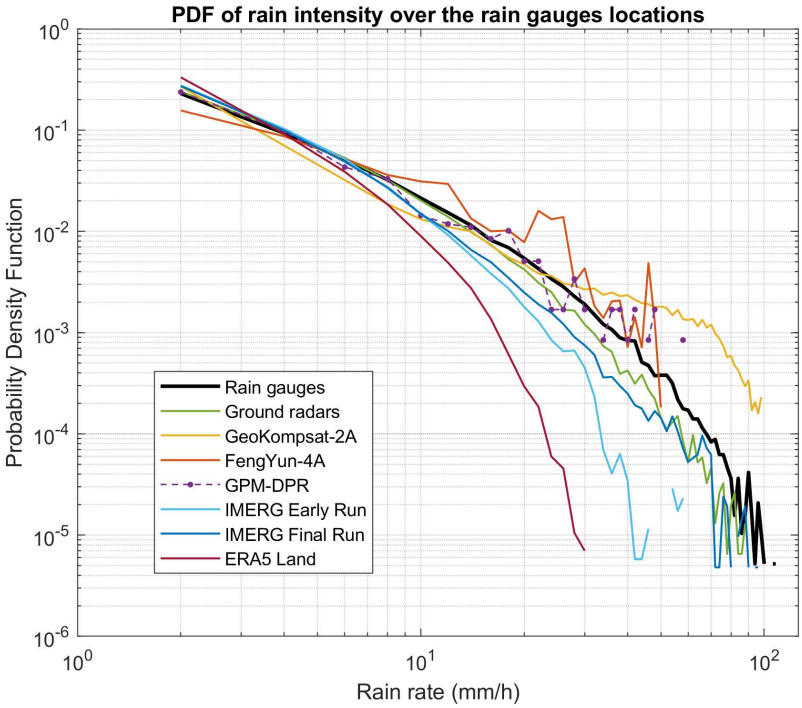


**Figure 6.** Distributions of measured/estimated precipitation along the full spectrum of intensity, or probability density functions (PDFs). Areas under the curves are normalized to 1. GPM-DPR distribution is marked by single points connected by a dashed line, in the effort to relate its different sample size and also overcome its intrinsic noisiness.

The AWS data (black line) span continuously from 1 to 100 mm/h, exhibiting a smooth curve. The minor fluctuations observed at the highest rainfall rates are likely to be attributed to noise given the relatively small sample size. The radar data (green line) show a close agreement with the AWS measurements, displaying a similar trend and level of noise. However, noticeable underestimation emerges above 10 mm/h, and increases for higher rainfall rates. The PDF of the GPM-DPR is depicted by purple points connected by a dashed line instead of a solid line to remark its notably smaller sample size compared to the other products. The PDF of GPM-DPR shows similarities with the gauges' PDF up until around 35 mm/h, after which it starts to overestimate. Notably, the statistical representativeness of the tail at high rain rates is low, with fewer than five data points at a probability density below $10^{-3}$.

Estimations from geostationary satellites show more discrepancy with the reference distribution. The GK-2A (yellow line) slightly overestimates the first rain rate class, followed by underestimation of low and medium rain rates, resulting in the lowest PDF values between 3 and 7 mm/h. Around 12 mm/h, the GK-2A aligns with the reference distribution (AWS) but then beyond 25 mm/h, it starts to overestimate, with discrepancies of up to an order of magnitude for the highest intensities. FY-4A (orange line) exhibits a different behavior for low intensities. It underestimates just the first intensity class and overestimates the remaining spectrum, with noticeable peaks that cannot be solely attributed to statistical noise. The estimations cease with a cut-off; no values were registered beyond 50 mm/h. The IMERG-Early run (light blue line) does not provide estimates for peak rainfall rates as indicated by the decline in the PDF above 30 mm/h and the absence of values above 65 mm/h. IMERG-Final run (dark blue line) instead shows a PDF that fairly aligns with the AWS reference up to 100 mm/h, with underestimation. The PDF of ERA5-Land initially shows good agreement with the reference for rain rates below 10 mm/h. However, ERA5-Land displays a notable decrease in probability above 15–20 mm/h. This indicates a

significant underestimation of medium and high rain intensities, likely due to the lower ground resolution of the product and its spatially distributed nature.

### *4.4. High-Resolution Rain Rate Estimates*

The seven products were then compared with the reference measurements at the highest level of spatial and temporal detail within our framework. The comparison was conducted across all the considered hours (702) and grid boxes (1229), again excluding the no-rain samples according to the AWS reference. The results are presented in Table 7.

**Table 7.** Statistical indicators for the continuous validation. Best and worst performance results for each score are indicated with bold and italic fonts, respectively (except for GPM-DPR, which does not share the same sample size). Ideal target scores are indicated in Table 5.

| Product | CC | CV | ME | MAE | $P_{50}$ | mKGE | $\frac{\sigma_e/\mu_e}{\sigma_o/\mu_o}$ |
|---|---|---|---|---|---|---|---|
| Radars | **0.70** | **1.38** | −0.34 | **0.56** | **0.75** | **0.53** | 1.13 |
| GK-2A | *0.29* | *3.16* | **0.07** | 1.32 | 0.39 | *0.09* | *1.55* |
| FY-4A | 0.3 | 2.62 | 0.33 | *1.42* | 0.66 | 0.23 | 0.98 |
| IMERG-Early run | 0.38 | 1.82 | *−0.50* | 0.86 | 0.5 | 0.21 | **1.00** |
| IMERG-Final run | 0.42 | 1.83 | −0.31 | 0.86 | 0.5 | 0.34 | 1.04 |
| ERA5-Land | 0.29 | 1.86 | −0.43 | 0.85 | *0.28* | 0.12 | 0.69 |
| GPM-DPR * | 0.44 | 2.67 | −0.21 | 0.78 | 0.75 | −0.17 | 2.00 |

* Sample size is constant for all products except GPM-DPR, for which it is 99% smaller.

The comparison can be visualized through the logarithmic density scatterplots presented in Figure 7. It has to be noted that, below 1 mm/h, the logarithmic binning becomes finer than the instrumental sensitivity of AWS (mainly 0.2 mm/h, a few 0.1 mm/h). This leads to the separated peaks observed in the histogram of Figure 7a and consequently to the vertical bands seen at the left margin of panels b to h.

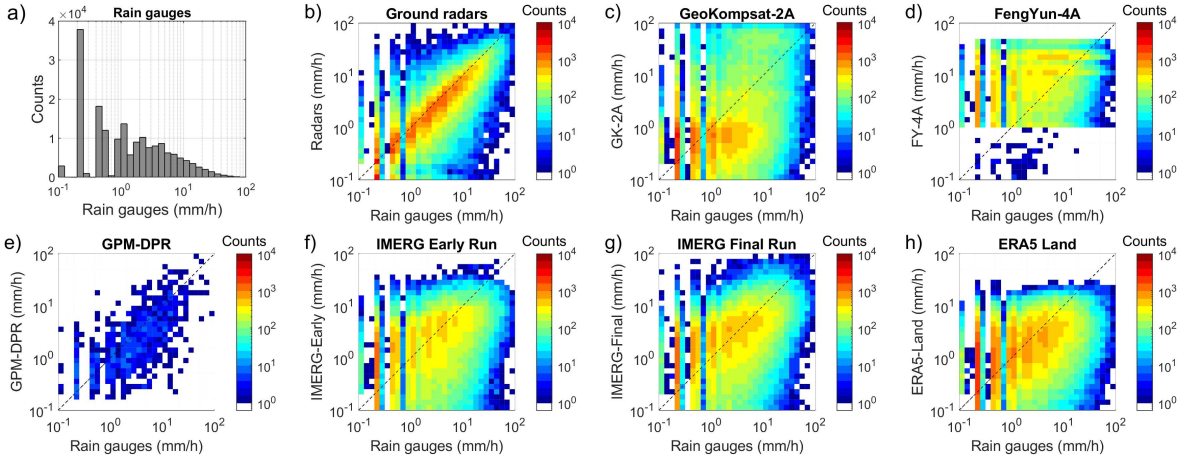


**Figure 7.** Comparison of each product (y-axis) against the AWS reference (x-axis) during all considered hours (702) over all the selected grid boxes (1229), excluding dry AWS samples. (**a**) Histogram of reference data from AWS. (**b**–**h**) Density scatterplots of all products (y-axis) against the corresponding AWS measurements (x-axis): radars (**b**); GK-2A (**c**); FY-4A (**d**); GPM-DPR (**e**); IMERG-Early run (**f**); IMERG-Final run (**g**); ERA5-Land (**h**). All axes are logarithmic.

By examining the mean absolute error (MAE), we can identify three distinct groups of products: radar-based ones (radars and GPM-DPR) with MAE below 0.8, integrated products (IMERG-Early run, IMERG-Final run, and ERA5-Land) with MAE around 0.85, and geostationary products (GK-2A and FY-4A) with MAE above 1.3.

Radars demonstrate the strongest correlation (CC = 0.7) and the lowest dispersion (CV = 1.38) and absolute errors (MAE = 0.56). Even though their data points are spread

across the entire scatterplot area (Figure 7b), the region along the diagonal of the plot is clearly more populated. A slight underestimation pattern is present, anticipated by the PDF analysis and confirmed by the mean error (ME = −0.34). There are some data points skewed towards the axes, representing certain misses and false alarms, but these branches are only one or two pixels wide. The performance of the GPM-DPR falls behind that of radars (CC = 0.44, CV = 2.67, and MAE = 0.78), but it still outperforms the geostationary estimates, though its small sample size is evident from the plot (Figure 7e), and thus its scores are to be taken cautiously.

Both geostationary products (Figure 7c,d) show very low correlation (CC = 0.3), the highest variation, and highest absolute errors. Data points are mostly located outside the region along the diagonal of the scatterplots. However, the dual behavior of GK-2A, which underestimates at medium rainfall rates but overestimates at high rainfall rates, somewhat balances out, resulting in the lowest overall mean error of the batch (ME = 0.07). In the case of FY-4A, certain values appear more frequently than others, creating band-like patterns in the scatterplot, which are consistent with the peaks noted in the PDF previously. Furthermore, the FY-4A precipitation estimates are mostly limited to the range of 1 to 50 mm/h, with apparent cut-offs and only a few outliers.

Early and Final runs of IMERG have slightly better correlation (CC = 0.38 and 0.42 respectively) than ERA5-Land (CC = 0.29). All three of them are affected by significant underestimation (ME between −0.3 and −0.5) and moderate dispersion (CV > 1.8). This is clearly visible in the scatterplots, in terms of deviation from the reference data (Figure 7f–h), although it is smaller than the one of geostationary products. The Final run data points are more balanced across the diagonal and more concentrated along it, particularly for rain rates below 10 mm/h. ERA5-Land has no estimates exceeding 30 mm/h.

Other Metrics: mKGE and $P_{50}$

Radars demonstrated favorable performance also in terms of the Modified Kling–Gupta Efficiency (mKGE = 0.53) and of the probability of providing an estimate within 50% of the reference ($P_{50}$ = 0.75). In contrast, ERA5-Land yielded low scores for both metrics. Interestingly, FY-4A outperformed GK-2A in these metrics, despite being quite similar in other aspects. In the case of DPR, while it exhibited the highest $P_{50}$ score, comparable to radars, it scored the lowest mKGE. The transition from the Early run to the Final run of the IMERG products showed a clear improvement in mKGE, but the $P_{50}$ remained unchanged.

Figure 8 illustrates the 3D decomposition of mKGE for the seven products. It is evident that the radar product (green dot) had a notable issue with general underestimation in the mean values (falling below the blue plane). However, its variance aligned closely with that of the reference (black line), and it exhibited the highest correlation. The IMERG products displayed variances that were also aligned with the reference, but both lacked correlation. Transitioning from the Early run to the Final run only resulted in slight improvements in the overall average. The GPM-DPR product showed instead a fair correlation and averages ratio, but its estimations exhibited twice the variation observed in the reference rainfall field. This factor significantly impacted the overall mKGE score for GPM-DPR. Both geostationary products demonstrated poor correlation with the reference. Similar to the categorical scores, they displayed contrasting skills: GK-2A exceeded the standard deviation but closely aligned with the mean, while FY-4A overestimated the mean value but demonstrated a standard deviation consistent with the reference. ERA5-Land was the only product that exhibited smoother results (lower variance) compared to the rain gauges.

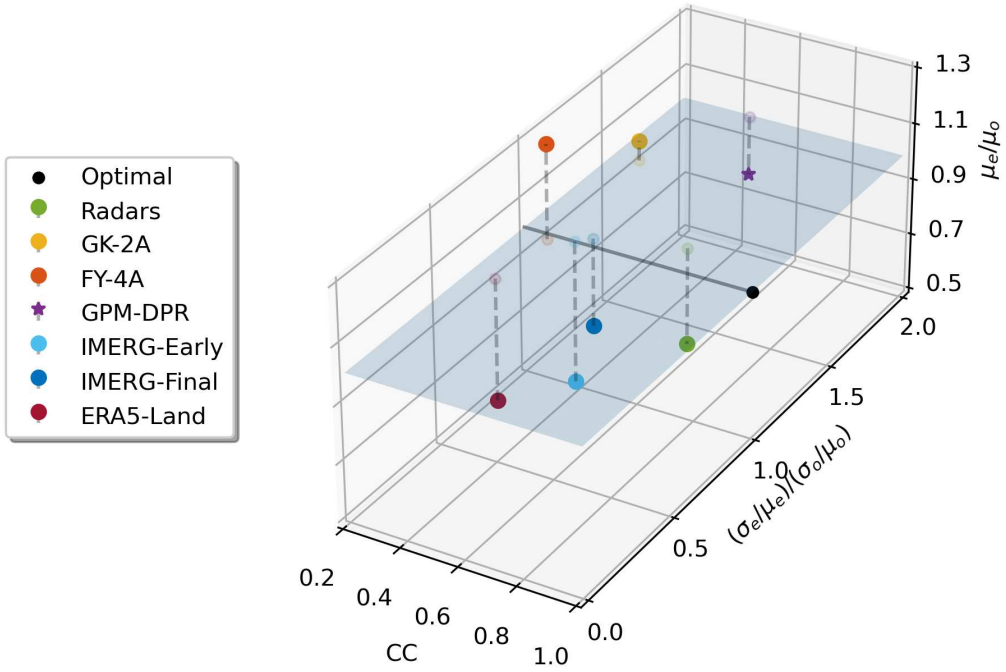


**Figure 8.** mKGE decomposition visualized in an Euclidean 3D space. Optimal point $(1,1,1)$ is shown with a black dot. The axis $(CC,1,1)$ is marked with a black line. The plane $\mu_e/\mu_o = 1$ is colored in partially transparent blue. Projections of the data points over this plane are the lighter semi-transparent dots, and the projection lines are dashed.

### *4.5. Sensitivity Analysis*

The trends of eight statistical scores, calculated for various categorical rain/no-rain thresholds are depicted in Figure 9, showing how the performance of the different products varies across different rainfall intensities.

With regard to rain detection (ETS), all instruments except the geostationary ones performed best at rain rates around 1 or 2 mm/h, and their quantitative absolute errors (MAE) remained relatively constant across all rainfall intensities. The False Alarm Rate (FAR) tended to worsen with increasing thresholds, while the probability of detection (POD) reached a peak between 0.2 and 2 mm/h for most products, except for ERA5-Land and GK-2A. Radars consistently underestimated precipitation at all rain rates but again exhibited the strongest correlation with AWS. They showed similar POD, FAR, and ETS to the GPM-DPR. The geostationary products displayed distinct error patterns in terms of quantitative indicators (Figure 9e–h), characterized by higher errors and overestimation at rain rates below 10 mm/h. However, both the mean error (ME) and MAE decreased with increasing thresholds, surpassing the skills of IMERG-Final run, ERA5-Land, and GPM-DPR above 10 mm/h. Geostationary estimates demonstrated significant variability in their detection skills structure (Figure 9a–d): GK-2A exhibited a clear tendency to overestimate occurrences of low rain rates (a tendency shared with ERA5-Land), with high POD and decreasing mBIAS as the threshold increased up to 3 mm/h. FY-4A started with a mBIAS below one that steadily increased, and its POD trend was more similar to that of radars and GPM-DPR, reaching a peak around 1 mm/h. The ETS, MAE, and CV of ERA5-Land were all very similar to those of both IMERG products.

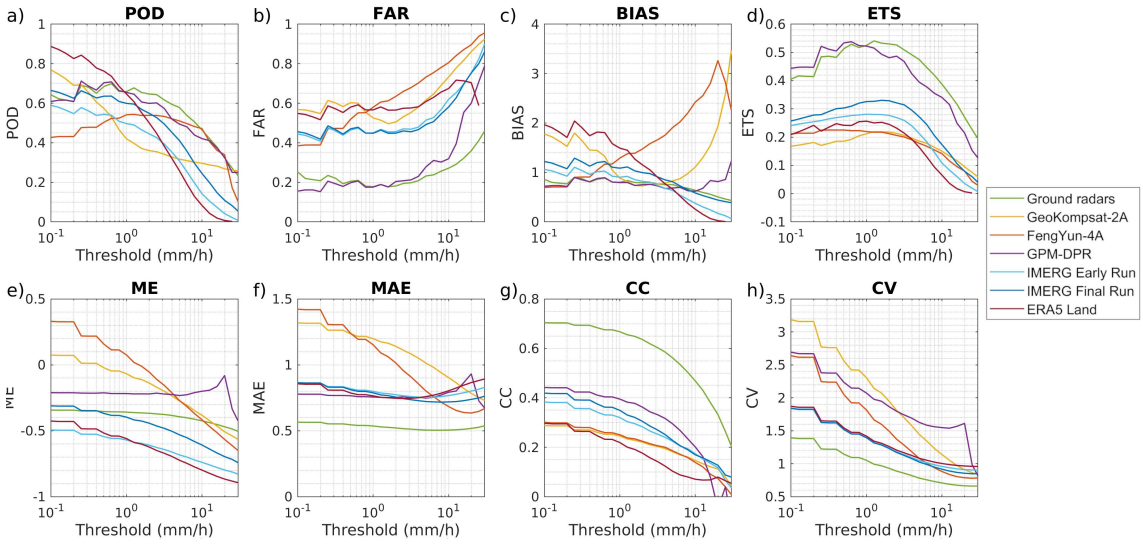


**Figure 9.** Trends of a subset of categorical and continuous indicators varying rain/no-rain thresholds from 0.1 to 30 mm/h: (**a**) POD; (**b**) FAR; (**c**) mBIAS; (**d**) ETS; (**e**) ME; (**f**) MAE; (**g**) CC; (**h**) CV.

## 5. Discussion

This study focuses on the validation of precipitation products at high spatial and temporal resolution during a series of intense phenomena of heavy and localized precipitation that occurred over Vietnam during the 2020 Typhoon season. On 1 August 2020, at 21:00 UTC, a well-developed precipitation structure was captured simultaneously by all the analyzed products (as depicted in Figure 3). This event coincided with the tropical storm Sinlaku, reaching its maximum intensity over the sea near the coast of Vietnam, subsequently making landfall.

The space-borne GPM-DPR product (Figure 3e) captured the core of the precipitation structure with significantly more detail and higher rain intensities compared to what was measured by radars (Figure 3b) and AWS (Figure 3a). Radars estimates may have been impacted by attenuation caused by heavy precipitation as likely indicated by the circular artifacts observed. The presence of a single instrument in close proximity to the most intense precipitation core, as appears from the map in Figure 1, is consistent with this scenario. Additionally, the localized and short-lived maxima may not have been captured by the rain gauges. Ground calibration could be used to enhance the GPM-DPR representation of rainfall (similar to what is observed with IMERG-Final run in Figure 3g). However, the unique advantage of GPM-DPR lies in its ability to provide detailed information about the fine structure of precipitation without the artifacts that arise from a ground-based perspective. This capability sets it apart from all other products analyzed in the study.

The ERA5-Land was included to assess the performance of model-based precipitation products. However, it is important to note that the values provided by ERA5-Land, which represent rain amounts uniformly distributed over the ground, do not necessarily align well with the values obtained from ground point measurements. The smoothness observed in the rainfall field on the map can be attributed to the coarse-grid (Figure 3h): recent studies have reaffirmed the challenges faced by model-based precipitation products in subtropical and tropical monsoon climate regions [44]. When analyzing rain maps aggregated over the entire period, it becomes evident that ERA5-Land fails to accurately reproduce high rainfall intensities.

The performance of geostationary satellites was found to be the poorest among the analyzed data sources. The underestimation of moderate rainfall intensities by GK-2A can be attributed to general intrinsic limitations of the IR remote sensing technique. On the other hand, the overestimation of the highest rainfall intensities may be a result of the calibration carried out with GPM-DPR products as it has also been reported in recent studies [27]. However, the error patterns observed in GK-2A cannot be completely generalized to other

geostationary estimates. For instance, FY-4A exhibited contrasting behavior, overestimating moderate-to-high rainfall rates ranging from 10 to 40 mm/h, while underestimating the highest rainfall values. Recent studies have documented similarly low overall performance results (low CC, POD, and mKGE) of the FY-4A precipitation estimate, not only over Vietnam but also over Japan and China [27,45,46]. In Figure 3, specifically panels c and d, it becomes apparent that the two satellites attribute the highest intensity rainfall to different regions within the cloud system: FY-4A predominantly assigns these intensities to the center or upper right of the storm core, whereas GK-2A focuses on the outer ring. Upon closer examination of the FY-4A map, discontinuities in rain intensity values are clearly visible along geographical parallels and meridians. In contrast, for GK-2A, it is evident that almost the entire map is covered by very small but non-zero rainfall estimates as confirmed by subsequent categorical scores. This led to GK-2A (and ERA5-Land) exhibiting a high POD and high FAR, particularly at lower rain/no-rain threshold values (as shown in Figure 9). However, when examining the maps of mean estimates (Figures 4 and 5, specifically panels c and d), certain similarities between the two geostationary products become apparent. Both products tend to overestimate mean precipitation in the same regions due to the cloud opacity in the IR.

IMERG Early run, GK-2A and GPM-DPR exhibit discrepancies that could be addressed through the incorporation of local measurements. The IMERG-Final run was the exception in that it utilizes local measurements already; however, it suffers from a significant latency of 3.5 months, making it evidently unsuitable for near real-time applications. Furthermore, even with calibration, the correlation at high temporal resolutions (i.e., hourly) remains a challenge if local high-resolution instruments like radars are not included in the calibration process as also reported by [47].

Among the analyzed data sources, radars demonstrated the highest level of correlation at the hourly scale. While they exhibit some underestimation, this issue can be mitigated through calibration techniques that effectively compensate for quantitative bias.

## 6. Conclusions

The aim of this work was to investigate how the rainfall associated with the extreme meteorological events of Autumn 2020 in Vietnam was seen by the precipitation estimation products currently available over the region. To achieve this, we built a framework that enabled qualitative and quantitative analyses of errors and uncertainties with high spatial and temporal detail. This procedure can be also applied to other regions, provided that reliable reference data are available.

For quantitative reference, in Vietnam we utilized a network comprising approximately 1200 tipping-bucket rain gauges. Next, various rainfall products were obtained from multiple sources, including the Vietnamese ground weather radar network, the IMERG-Early run and Final run datasets, the South Korean GEO-KOMPSAT-2A satellite, the Chinese FengYun-4A geostationary satellite, the Dual frequency Precipitation Radar on the GPM-CO satellite, and the ERA5-Land reanalysis. All of these products were rescaled onto a $0.02^\circ \times 0.02^\circ$ grid and then compared against the AWS measurements over the matching grid cells (1229). This analysis covered six instances of heavy rain events that occurred in 2020, spanning over 29 days (702 h), and encompassing more than $6 \times 10^5$ data points.

The results indicate that the radars product is more capable of reproducing the reference data during intense phenomena than all other products, with a CC value of 0.70 and a normalized RMSD (or CV) of 1.38. However, it displayed some underestimation in both rain detection (mBIAS = 0.77) and retrieval (ME = $-0.34$), consistently with the expectations about the radar attenuation issues due to heavy rainfall. GPM-DPR demonstrated an even higher ETS value of 0.45 compared to 0.41 of the radar data, but its sample size is strongly limited by the few GPM-CO satellite overpasses in the region during the selected events. The geostationary products overestimated both the intensity and occurrence of precipitation, resulting in high errors and the lowest ETS values. In contrast, the multi-satellite

products of IMERG performed better, although they failed to reproduce the highest rainfall intensities registered during the extreme events.

The study we conducted was limited to a single typhoon season, which was chosen for its particular intensity. During this period, nine tropical cyclones of varying characteristics and peak intensities were observed with an hourly resolution as they passed over Vietnam. Despite the specificity of our study, the findings suggest that global products fall short in accurately depicting high-resolution precipitation patterns, particularly during severe or extreme precipitation events tied to the evolution of tropical cyclones. The available products sometimes show complementary performance results, suggesting that a synergistic use of satellite and ground networks estimates can improve the accuracy, spatial and temporal resolution and latency of precipitation products.

**Supplementary Materials:** The following supporting information can be downloaded at: https://www.mdpi.com/article/10.3390/rs16050805/s1, S1: Probability density function (PDF) of the precipitation: focus on the lowest values; S2: Orography of Vietnam mainland; S3: Typhoon tracks of the 2020 storm season.

**Author Contributions:** Conceptualization: T.T.N.N. and F.P.; methodology: F.P.; software, W.C., M.P. and G.R.; validation: M.P. and G.R.; resources: T.T.N.N., T.V.N. and W.C.; writing—original draft preparation: G.R.; writing—review and editing: W.C., T.T.N.N., M.P., D.C., F.P., and G.R.; visualization: M.P., D.C. and G.R.; project administration: F.P.; funding acquisition: F.P. All authors have read and agreed to the published version of the manuscript.

**Funding:** This research was conducted inside the INDRA Project (research and development of INtegrateD RAinfall measurements platform for application in agriculture, hydro - meteorological hazard prevention and mitigation and water management) which was funded by the Italian Ministry of Foreign Affairs and International Cooperation under the Projects of major importance in the Scientific and Technological Collaboration Executive Programmes, and by the Vietnam Ministry of Science and Technology, under the Italy—Vietnam bilateral project code NDT/IT/22/07.

**Data Availability Statement:** AWS and Radars data presented in this study are available upon request from the lead author. GK-2A data are downloadable freely through the KMA/NMSC Open API (https://nmsc.kma.go.kr/ (accessed on 27 December 2023)) after requesting membership through an application form. FY-4A data are available free of charge upon registration at the FENGYUN Satellite Data Center (https://satellite.nsmc.org.cn/ (accessed on 27 December 2023)). IMERG and GPM-DPR data are available at the Precipitation Data Directory (https://gpm.nasa.gov/data/directory (accessed on 27 December 2023)) upon registration. ERA5 data can be downloaded upon registration through the Climate Data Store (https://cds.climate.copernicus.eu/ (accessed on 27 December 2023)).

**Acknowledgments:** The authors thank Marco Abbiati (Scientific Attaché of the Italian Embassy in Hanoi) for his continuous support and availability throughout the INDRA Project.

**Conflicts of Interest:** The authors declare no conflicts of interest. The funders had no role in the design of the study; in the collection, analyses, or interpretation of data; in the writing of the manuscript; or in the decision to publish the results.

## Abbreviations

The following abbreviations are used in this manuscript:

| | |
|---|---|
| AGRI | Advanced Geosynchronous Radiation Imager |
| AMI | Advanced Meteorological Imager |
| AWS | Automatic Weather Station |
| mBIAS | Multiplicative bias (categorical) |
| CC | Correlation Coefficient |
| CHIRPS | Climate Hazards Group InfraRed Precipitation with Station data |
| CMORPH | Climate Prediction Center Morphing Technique |
| CSI | Critical Success Index |
| DPR | Dual-frequency Precipitation Radar (active sensor) |

| | |
|---|---|
| ECMWF | European Centre for Medium-range Weather Forecasts |
| ERA5-Land | ECMWF ReAnalysis ver. 5 |
| ETS | Equitable Threat Score |
| FAR | False Alarm Ratio |
| FY-4A | Fengyun 4A |
| GEO | Geostationary Earth orbit |
| GK-2A | GEO-KOMPSAT-2A |
| GPCC | Global Precipitation Climatology Centre |
| GPM | Global Precipitation Mission |
| GPM-CO | Global Precipitation Mission Core Observatory |
| GSMaP | Global Satellite Mapping of Precipitation |
| IMERG | Integrated Multi-satellitE Retrievals, version 06 |
| IR | Infra-Red passive sensor |
| JAXA | Japan Aerospace Exploration Agency |
| JMA | Japan Meteorological Agency |
| JWA | Japan Weather Association |
| KMA | Korean Meteorological Administration |
| LEO | Low Earth Orbit |
| MAE | Mean Absolute Error |
| ME | Mean Error or relative bias |
| mKGE | Modified Kling–Gupta Efficiency |
| MW | MicroWave passive sensor |
| NASA | National Aeronautics and Space Administration |
| NCN | National Centre for Hydro-Meteorological Network |
| NRT | Near Real-Time |
| $P_{50}$ | Probability to find the estimate inside 50% of the observation |
| POD | Probability Of Detection |
| QPE | Quantitative Precipitation Estimation |
| RG | Rain Gauge |
| RMSD | Root Mean Square Deviation |
| TRMM | Tropical Rainfall Measuring Mission |
| VNMHA | The Vietnam Meteorological and Hydrological Administration |

## References


1. Luu, L.N.; Scussolini, P.; Kew, S.; Philip, S.; Hariadi, M.H.; Vautard, R.; Van Mai, K.; Van Vu, T.; Truong, K.B.; Otto, F.; et al. Attribution of typhoon-induced torrential precipitation in Central Vietnam, October 2020. *Clim. Chang.* **2021**, *169*, 24. [CrossRef]
2. Ortiz-Vargas, A.; Sebesvari, Z. Technical Report: Floods in Central Viet Nam. In *Interconnected Disaster Risks 2020/2021*; United Nations University-Institute for Environment and Human Security (UNU-EHS): Bonn, Germany , 2021. [CrossRef]
3. Puca, S.; Porcu', F.; Rinollo, A.; Vulpiani, G.; Baguis, P.; Balabanova, S.; Campione, E.; Ertürk, A.; Gabellani, S.; Iwanski, R.; et al. The validation service of the hydrological SAF geostationary and polar satellite precipitation products. *Nat. Hazards Earth Syst. Sci.* **2014**, *14*, 871–889. [CrossRef]
4. Schwaller, M.R.; Morris, K.R. A Ground Validation Network for the Global Precipitation Measurement Mission. *J. Atmos. Ocean. Technol.* **2011**, *28*, 301–319. [CrossRef]
5. Kidd, C.; Shige, S.; Vila, D.; Tarnavsky, E.; Yamamoto, M.K.; Maggioni, V.; Maseko, B., The IPWG Satellite Precipitation Validation Effort. In *Satellite Precipitation Measurement: Volume 2*; Springer International Publishing: Cham, Switzerland, 2020; pp. 453–470. [CrossRef]
6. Dos Reis, J.B.C.; Rennó, C.D.; Lopes, E.S.S. Validation of Satellite Rainfall Products over a Mountainous Watershed in a Humid Subtropical Climate Region of Brazil. *Remote Sens.* **2017**, *9*, 1240. [CrossRef]
7. Deo, A.; Munchak, S.J.; Walsh, K.J.E. Cross Validation of Rainfall Characteristics Estimated from the TRMM PR, a Combined PR–TMI Algorithm, and a C-POL Ground Radar during the Passage of Tropical Cyclone and Nontropical Cyclone Events over Darwin, Australia. *J. Atmos. Ocean. Technol.* **2018**, *35*, 2339–2358. [CrossRef] [PubMed]
8. Dandridge, C.; Lakshmi, V.; Bolten, J.; Srinivasan, R. Evaluation of Satellite-Based Rainfall Estimates in the Lower Mekong River Basin (Southeast Asia). *Remote Sens.* **2019**, *11*, 2709. [CrossRef]
9. Stephens, C.M.; Pham, H.T.; Marshall, L.A.; Johnson, F.M. Which Rainfall Errors Can Hydrologic Models Handle? Implications for Using Satellite-Derived Products in Sparsely Gauged Catchments. *Water Resour. Res.* **2022**, *58*, e2020WR029331. [CrossRef]
10. Gummadi, S.; Dinku, T.; Shirsath, P.B.; Kadiyala, M.D.M. Evaluation of multiple satellite precipitation products for rainfed maize production systems over Vietnam. *Sci. Rep.* **2022**, *12*, 485. [CrossRef] [PubMed]
11. Nguyen, T.H.; Masih, I.; Mohamed, Y.A.; Van der Zaag, P. Validating Rainfall-Runoff Modelling Using Satellite-Based and Reanalysis Precipitation Products in the Sre Pok Catchment, the Mekong River Basin. *Geosciences* **2018**, *8*, 164. [CrossRef]

12. Mohammed, I.N.; Bolten, J.D.; Srinivasan, R.; Lakshmi, V. Satellite observations and modeling to understand the Lower Mekong River Basin streamflow variability. *J. Hydrol.* **2018**, *564*, 559–573. [CrossRef]
13. Yuan, F.; Zhang, L.; Win, K.W.W.; Ren, L.; Zhao, C.; Zhu, Y.; Jiang, S.; Liu, Y. Assessment of GPM and TRMM Multi-Satellite Precipitation Products in Streamflow Simulations in a Data-Sparse Mountainous Watershed in Myanmar. *Remote Sens.* **2017**, *9*, 302. [CrossRef]
14. Gunathilake, M.B.; Zamri, M.N.M.; Alagiyawanna, T.P.; Samarasinghe, J.T.; Baddewela, P.K.; Babel, M.S.; Jha, M.K.; Rathnayake, U.S. Hydrologic Utility of Satellite-Based and Gauge-Based Gridded Precipitation Products in the Huai Bang Sai Watershed of Northeastern Thailand. *Hydrology* **2021**, *8*, 165. [CrossRef]
15. Xia, X.; Liu, Y.; Jing, W.; Yao, L. Assessment of Four Satellite-Based Precipitation Products Over the Pearl River Basin, China. *IEEE Access* **2021**, *9*, 97729–97746. [CrossRef]
16. Li, R.; Shi, J.; Ji, D.; Zhao, T.; Plermkamon, V.; Moukomla, S.; Kuntiyawichai, K.; Kruasilp, J. Evaluation and Hydrological Application of TRMM and GPM Precipitation Products in a Tropical Monsoon Basin of Thailand. *Water* **2019**, *11*, 818. [CrossRef]
17. Yuan, F.; Zhang, L.; Soe, K.M.W.; Ren, L.; Zhao, C.; Zhu, Y.; Jiang, S.; Liu, Y. Applications of TRMM- and GPM-Era Multiple-Satellite Precipitation Products for Flood Simulations at Sub-Daily Scales in a Sparsely Gauged Watershed in Myanmar. *Remote Sens.* **2019**, *11*, 140. [CrossRef]
18. Trinh-Tuan, L.; Matsumoto, J.; Ngo-Duc, T.; Nodzu, M.I.; Inoue, T. Evaluation of satellite precipitation products over Central Vietnam. *Prog. Earth Planet. Sci.* **2019**, *6*, 54. [CrossRef]
19. Mohsan, M.; Acierto, R.A.; Kawasaki, A.; Zin, W.W. Preliminary Assessment of GPM Satellite Rainfall over Myanmar. *J. Disaster Res.* **2018**, *13*, 22–30. [CrossRef]
20. Luong, B.N.; Van, Q.D. Accuracy of Integrated Multi-SatelliE Retrievals for GPM Satellite Rainfall Product over North Vietnam. *Pol. J. Environ. Stud.* **2021**, *30*, 5657–5667. [CrossRef]
21. Nodzu, M.I.; Jun, M.; Long, T.T.; Ngo-Duc, T. Precipitation estimation performance by Global Satellite Mapping and its dependence on wind over northern Vietnam. *Prog. Earth Planet. Sci.* **2019**, *6*, 58. [CrossRef]
22. Le, H.M.; Sutton, J.R.P.; Bui, D.D.; Bolten, J.D.; Lakshmi, V. Comparison and Bias Correction of TMPA Precipitation Products over the Lower Part of Red–Thai Binh River Basin of Vietnam. *Remote Sens.* **2018**, *10*, 1582. [CrossRef]
23. Hai, B.T.; Tuan, N.V. Nghiên cứu đánh giá và so sánh các đữ liệu mưa vệ tinh độ phân giải cao lưu vực sông Cả. *Vietnam J. Hydrometeorol.* **2018**, *11*, 695. Available online: https://vjol.info.vn/index.php/TCKHTV/article/view/59946 (accessed on 9 November 2023).
24. Le, M.H.; Lakshmi, V.; Bolten, J.; Bui, D.D. Adequacy of Satellite-derived Precipitation Estimate for Hydrological Modeling in Vietnam Basins. *J. Hydrol.* **2020**, *586*, 124820. [CrossRef]
25. Tran, T.N.D.; Le, M.H.; Zhang, R.; Nguyen, B.Q.; Bolten, J.D.; Lakshmi, V. Robustness of gridded precipitation products for vietnam basins using the comprehensive assessment framework of rainfall. *Atmos. Res.* **2023**, *293*, 106923. [CrossRef]
26. Petracca, M.; D'Adderio, L.P.; Porcu', F.; Vulpiani, G.; Sebastianelli, S.; Puca, S. Validation of GPM Dual-Frequency Precipitation Radar (DPR) Rainfall Products over Italy. *J. Hydrometeorol.* **2018**, *19*, 907–925. [CrossRef]
27. Yin, G.; Baik, J.; Park, J. Comprehensive analysis of GEO-KOMPSAT-2A and FengYun satellite-based precipitation estimates across Northeast Asia. *GIScience Remote Sens.* **2022**, *59*, 782–800. [CrossRef]
28. Huffman, G.J.; Bolvin, D.T.; Braithwaite, D.; Hsu, K.L.; Joyce, R.J.; Kidd, C.; Nelkin, E.J.; Sorooshian, S.; Stocker, E.F.; Tan, J.; et al. Integrated Multi-satellite Retrievals for the Global Precipitation Measurement (GPM) Mission (IMERG). In *Satellite Precipitation Measurement: Volume 1*; Springer International Publishing: Cham, Switzerland, 2020; pp. 343–353. [CrossRef]
29. Muñoz Sabater, J.; Dutra, E.; Agustí-Panareda, A.; Albergel, C.; Arduini, G.; Balsamo, G.; Boussetta, S.; Choulga, M.; Harrigan, S.; Hersbach, H.; et al. ERA5-Land: A state-of-the-art global reanalysis dataset for land applications. *Earth Syst. Sci. Data* **2021**, *13*, 4349–4383. [CrossRef]
30. Muñoz Sabater, J. *ERA5-Land Hourly Data from 1950 to Present*; Copernicus Climate Change Service (C3S) Climate Data Store (CDS): 2019. Available online: https://cds.climate.copernicus.eu/cdsapp#!/dataset/10.24381/cds.e2161bac?tab=overview (accessed on 9 November 2023).
31. Makihara, Y. A Method for Improving Radar Estimates of Precipitation by Comparing Data from Radars and Raingauges. *J. Meteorol. Soc. Jpn. Ser. II* **1996**, *74*, 459–480. [CrossRef]
32. Kimpara, C.; Tonouchi, M.; Hoa, B.T.K.; Hung, N.V.; Cuong, N.M.; Akaeda, K. Quantitative Precipitation Estimation by Combining Rain gauge and Meteorological Radar Network in Viet Nam. *VN J. Hydrometeorol.* **2020**, *5*, 36–50. [CrossRef]
33. Iguchi, T.; Seto, S.; Meneghini, R.; Yoshida, N.; Awaka, J.; Le, M.; Chandrasekar, V.; Brodzik, S.; Kubota, T.; Takahashi, N. *GPM/DPR Level-2 Algorithm Theoretical Basis Document*; NASA GPM : 2021. Available online: https://gpm.nasa.gov/sites/default/files/2022-06/ATBD_DPR_V07A.pdf (accessed on 3 November 2023).
34. Hirose, H.; Shige, S.; Yamamoto, M.K.; Higuchi, A. High Temporal Rainfall Estimations from Himawari-8 Multiband Observations Using the Random-Forest Machine-Learning Method. *J. Meteorol. Soc. Jpn. Ser. II* **2019**, *97* , 2019–2040. [CrossRef]
35. Shin, D.; Seo, D.; Kim, D. *Algorithm Theoretical Basis Document, Rainfall Intensity*; National Meteorological Satellite Center, Korea Meteorological Administration; 2019. Available online: http://210.125.45.70/resources/common/pdf/GK2A_ATBD_RR_KOR_v1.0.pdf (accessed on 9 November 2023).
36. Yang, J.; Zhang, Z.; Wei, C.; Lu, F.; Guo, Q. Introducing the New Generation of Chinese Geostationary Weather Satellites, Fengyun-4. *Bull. Am. Meteorol. Soc.* **2017**, *98*, 1637–1658. [CrossRef]

37. NSMC-DataService. *Spectral Response Parameters of FY-4A Satellite*; National Satellite Meteorological Center, China Meteorological Administration; 2018. Available online: http://img.nsmc.org.cn/PORTAL/NSMC/DATASERVICE/SRF/FY4A/FY4A_AGRI_SRF_20180306.pdf (accessed on 9 November 2023).
38. Huffman, G.J.; Bolvin, D.T.; Braithwaite, D.; Hsu, K.; Joyce, R.; Kidd, C.; Nelkin, E.J.; Sorooshian, S.; Tan, J.; Xie, P. *NASA Global Precipitation Measurement (GPM) Integrated Multi-SatellitE Retrievals for GPM (IMERG), Algorithm Theoretical Basis Document (ATBD) Version 06*; NASA GPM; 2020. Available online: https://gpm.nasa.gov/sites/default/files/2020-05/IMERG_ATBD_V06.3.pdf (accessed on 9 November 2023).
39. Hersbach, H.; Bell, B.; Berrisford, P.; Hirahara, S.; Horányi, A.; Muñoz-Sabater, J.; Nicolas, J.; Peubey, C.; Radu, R.; Schepers, D.; et al. The ERA5 global reanalysis. *Q. J. R. Meteorol. Soc.* **2020**, *146*, 1999–2049. [CrossRef]
40. Nguyen, Q.; Renwick, J.; Mcgregor, J. Variations of surface temperature and rainfall in Vietnam from 1971 to 2010. *Int. J. Climatol.* **2014**, *34*, 249–264. [CrossRef]
41. Nurmi, P. Recommendations on the verification of local weather forecasts. *ECMWF Tech. Memo.* **2003**, *430*, 19. [CrossRef]
42. Gupta, H.V.; Kling, H.; Yilmaz, K.K.; Martinez, G.F. Decomposition of the mean squared error and NSE performance criteria: Implications for improving hydrological modelling. *J. Hydrol.* **2009**, *377*, 80–91. [CrossRef]
43. Kling, H.; Fuchs, M.; Paulin, M. Runoff conditions in the upper Danube basin under an ensemble of climate change scenarios. *J. Hydrol.* **2012**, *424–425*, 264–277. [CrossRef]
44. Xu, J.; Ma, Z.; Yan, S.; Peng, J. Do ERA5 and ERA5-land precipitation estimates outperform satellite-based precipitation products? A comprehensive comparison between state-of-the-art model-based and satellite-based precipitation products over mainland China. *J. Hydrol.* **2022**, *605*, 127353. [CrossRef]
45. Lu, H.; Huang, Z.; Ding, L.; Lu, T.; Yuan, Y. Calibrating FY4A QPE using CMPA over Yunnan–Kweichow Plateau in summer 2019. *Eur. J. Remote Sens.* **2021**, *54*, 476–486. [CrossRef]
46. Qiu, C.; Ding, L.; Zhang, L.; Xu, J.; Ma, Z. Quantitative Characteristics of the Current Multi-Source Precipitation Products over Zhejiang Province, in Summer, 2019. *Water* **2021**, *13*, 334. [CrossRef]
47. Ramadhan, R.; Yusnaini, H.; Marzuki, M.; Muharsyah, R.; Suryanto, W.; Sholihun, S.; Vonnisa, M.; Harmadi, H.; Ningsih, A.P.; Battaglia, A.; et al. Evaluation of GPM IMERG Performance Using Gauge Data over Indonesian Maritime Continent at Different Time Scales. *Remote Sens.* **2022**, *14*, 1172. [CrossRef]